Monthly Notices of the ROYAL ASTRONOMICAL SOCIETY

MNRAS **469,** 448–458 (2017) doi:10.1093/mnras/stx839
Advance Access publication 2017 April 5

No evidence for Population III stars or a direct collapse black hole in the $z = 6.6$ Lyman α emitter 'CR7'

R. A. A. Bowler,[1]★ R. J. McLure,[2] J. S. Dunlop,[2] D. J. McLeod,[2] E. R. Stanway,[3] J. J. Eldridge[4] and M. J. Jarvis[1,5]

[1]*Astrophysics, The Denys Wilkinson Building, University of Oxford, Keble Road, Oxford OX1 3RH, UK*
[2]*Institute for Astronomy, University of Edinburgh, Royal Observatory, Edinburgh EH9 3HJ, UK*
[3]*Department of Physics, University of Warwick, Gibbet Hill Road, Coventry CV4 7AL, UK*
[4]*Department of Physics, University of Auckland, Private Bag 92019, Auckland 1142, New Zealand*
[5]*Department of Physics, University of the Western Cape, Bellville 7535, South Africa*

Accepted 2017 April 3. Received 2017 March 14; in original form 2016 September 5

ABSTRACT

The $z = 6.6$ Lyman α emitter 'CR7' has been claimed to have a Population III (Pop III) like stellar population, or alternatively, be a candidate direct collapse black hole (DCBH). In this paper, we investigate the evidence for these exotic scenarios using recently available, deeper, optical, near-infrared and mid-infrared imaging. We find strong *Spitzer*/Infrared Array Camera detections for the main component of CR7 at 3.6 and 4.5 μm, and show that it has a blue colour ($[3.6] - [4.5] = -1.2 \pm 0.3$). This colour cannot be reproduced by current Pop III or pristine DCBH models. Instead, the results suggest that the [3.6] band is contaminated by the [O III]λλ 4959, 5007 emission line with an implied rest-frame equivalent width of $EW_0(H\beta + [O\,III]) \gtrsim 2000$ Å. Furthermore, we find that new near-infrared data from the UltraVISTA survey supports a weaker He II λ1640 emission line than previously measured, with $EW_0 = 40 \pm 30$ Å. For the fainter components of CR7 visible in *Hubble Space Telescope* imaging, we find no evidence that they are particularly red as previously claimed, and show that the derived masses and ages are considerably uncertain. In light of the likely detection of strong [O III] emission in CR7, we discuss other more standard interpretations of the system that are consistent with the data. We find that a low-mass, narrow-line active galactic nucleus can reproduce the observed features of CR7, including the lack of radio and X-ray detections. Alternatively, a young, low-metallicity ($\sim 1/200\,Z_\odot$) starburst, modelled including binary stellar pathways, can reproduce the inferred strength of the He II line and simultaneously the strength of the observed [O III] emission, but only if the gas shows supersolar α-element abundances ($O/Fe \simeq 5\,(O/Fe)_\odot$).

Key words: galaxies: evolution – galaxies: formation – galaxies: high-redshift.

1 INTRODUCTION

The Lyman α emission line at $\lambda_0 = 1216$ Å provides a unique probe of the progress and topology of reionization at $z > 6$ (e.g. Dijkstra et al. 2014). Using narrow-band surveys, it is possible to select large samples of Lyman-α-emitting galaxies (LAEs) up to $z \simeq 7$ (e.g. Ouchi et al. 2008, 2010; Matthee et al. 2015) and potentially to higher redshifts (e.g. Tilvi et al. 2010; Krug et al. 2012). Several of these narrow-band-selected galaxies at $z = 6.6$ have generated considerable interest due to their particularly strong ($\log_{10}[L_{Ly\alpha}/erg\,s^{-1}] > 43$) and extended (>10 kpc) Lyman α emission. The low-metallicity, triple-merger system 'Himiko' has been extensively studied (Ouchi et al. 2009, 2013; Zabl et al. 2015), and recently Sobral et al. (2015, hereafter S15) reported an even brighter LAE, 'CR7', which was found within the degree-scale Cosmic Origins Survey (COSMOS) field. CR7 was initially discovered during a search for Lyman-break galaxies in Bowler et al. (2012), and was independently selected by S15 in Subaru/Suprime-Cam narrow-band imaging (using the *NB*921 filter centred at 9210 Å). Follow-up spectroscopy confirmed the presence of a strong Lyman α emission line with a rest-frame equivalent width in excess of $EW_0 > 200$ Å. Near-infrared spectroscopy of CR7 also revealed an $\sim 6\sigma$ emission line attributed to He II λ1640. The He II line was observed to be sufficiently strong to boost the available *J*-band photometry by 0.4 mag (S15), with an inferred equivalent width of

★ E-mail: rebecca.bowler@physics.ox.ac.uk

© 2017 The Authors
Published by Oxford University Press on behalf of the Royal Astronomical Society

$EW_0 = 80 \pm 20$ Å. The strong and narrow He II line, coupled with the non-detection of metal lines in the near-infrared spectrum, has led to the interpretation that this galaxy has a Population III (Pop III) like stellar population (Pallottini et al. 2015; S15; Visbal, Haiman & Bryan 2016; Xu et al. 2016; Yajima & Khochfar 2016) or alternatively harbours an accreting direct collapse black hole (DCBH; Agarwal et al. 2016; Dijkstra, Gronke & Sobral 2016; Hartwig et al. 2016; Smidt, Wiggins & Johnson 2016; Smith, Bromm & Loeb 2016).

With high-resolution imaging from archival *Hubble Space Telescope* (*HST*) data, CR7 appears as three distinct clumps, with the Lyman α and He II emission peaking at the location of the brightest component (A). The two fainter objects (B and C) are separated from the A component by $\gtrsim$5 kpc (assuming that they are also at $z = 6.6$) and appear redder, leading to the interpretation that they are older (S15). In recent theoretical models of CR7, components B and C potentially provide the required ionizing photons to suppress star formation in component A at earlier times, leading to the formation of a pristine Pop III starburst (S15) or DCBH (Agarwal et al. 2016). In both scenarios, the presence of older companions is required to reproduce the observed rest-frame optical detections (in the *Spitzer* [3.6] and [4.5] bands), which are not predicted by the extremely blue Pop III or DCBH spectral energy distributions (SEDs). In simulations of potential sites of Pop III star formation, it has appeared challenging to recreate the properties of CR7 due primarily to the large mass ($\geq 10^7\,M_\odot$; S15; Visbal et al. 2016) of Pop III stars required to reproduce the Lyman α and He II luminosities (Pallottini et al. 2015; Hartwig et al. 2016; Xu et al. 2016). Another possible issue with the Pop III scenario is the short ($\lesssim$5 Myr) visibility time-scale of such a burst if it occurred (Hartwig et al. 2016). While the DCBH interpretation alleviates these concerns somewhat, with visibility time-scales of tens of Myr (Pallottini et al. 2015), the line luminosities require a system with a mass greater than the maximum mass thought to be created by direct collapse, requiring the pristine DCBH to have accreted substantially (Dijkstra et al. 2016; Smidt et al. 2016). Given the intense interest in CR7 and the exciting implications of the potential discovery of a Pop III starburst or a DCBH, it is important to scrutinize the observational evidence. While future observations with *HST* and the Atacama Large Millimeter/Sub-millimeter Array will provide further insights into the properties of CR7, it is possible to discern salient details about the system from currently available broad-band photometric data.

In this work, we present an analysis of the most recently available imaging data for CR7, which extends up to 1 mag deeper than that presented in S15. Crucially, this includes deeper near-infrared data from the third data release of the UltraVISTA survey and deeper *Spitzer* data at 3.6 and 4.5 μm. The data sets are described in detail in Section 2. Our analysis of the updated photometric data is presented in Section 3. In Section 4, we compare the observed *Spitzer*/Infrared Array Camera (IRAC) colours to those predicted by Pop III and DCBH models, where we find that neither model can reproduce the data. In light of our findings, we discuss alternative interpretations for the nature of CR7 in Section 5, which includes a comparison of the properties of CR7 to the BPASS (Binary Population and Spectral Synthesis) stellar population models (Eldridge, Izzard & Tout 2008; Eldridge & Stanway 2009). We end with our conclusions in Section 6. All magnitudes are quoted in the AB system (Oke 1974; Oke & Gunn 1983). At $z = 6.6$, a measured separation of 1 arcsec corresponds to a proper distance of 5.4 kpc assuming a cosmology with $\Omega_m = 0.3$, $\Omega_\Lambda = 0.7$ and $H_0 = 70\,km\,s^{-1}\,Mpc^{-1}$.

2 DATA

We use ground-based optical data in the *u*griz* bands from the Canada–France–Hawaii Telescope Legacy Survey, and *HST*/Advanced Camera for Surveys (ACS) I_{814} imaging taken as part of the COSMOS survey (Koekemoer et al. 2007). Deeper imaging in the z' band from Subaru/Suprime-Cam was also included (Furusawa et al. 2016). The ground-based near-infrared imaging analysed was from the third data release (DR3)[1] of the UltraVISTA survey (McCracken et al. 2012), which provides imaging in the $YJHK_s$ bands. In the COSMOS field, CR7 is located close to the edge of one of the 'ultra'-deep strips of the UltraVISTA survey, and hence has shallower depths by 0.2–0.4 mag than for the deeper regions quoted in Bowler et al. (2017). In addition to the ground-based imaging, *HST*/WFC3 data exist for CR7 in the YJ_{110} and H_{160} bands. These data were taken as part of an unrelated proposal (PI: Förster Schreiber, ID 12578). We independently reduced these data (see section 2.3 of Bowler et al. 2017 for details), matching the astrometry to the UltraVISTA imaging with a resulting accuracy of rms <0.1 arcsec. Finally, we used new mid-infrared imaging at 3.6 and 4.5 μm (hereafter denoted [3.6] and [4.5]) from the *Spitzer*/IRAC taken as part of the Spitzer Large Area Survey with Hyper-Suprime-Cam (SPLASH; Steinhardt et al. 2014). Further details of the image processing, including astrometric and photometric consistency checks performed on the ground-based data sets (which were also performed for the UltraVISTA DR3 images), can be found in Bowler et al. (2014). Errors on the photometry presented in this work were determined from empty aperture measurements. Using the segmentation map produced by SExtractor, we identified blank regions of the images and measured the flux in circular apertures of the appropriate diameter (1.2–3 arcsec) to match that used for the galaxy photometry. A local depth was then calculated for each point in the field by determining the standard deviation (with the median absolute deviation estimator) of the closest 200 apertures. This approach accounts for the correlated noise in the images by directly measuring the noise in a given aperture size.

In the selection and further analysis of CR7 presented in Matthee et al. (2015) and S15, the optical data utilized were from the Subaru/Suprime-Cam imaging of the COSMOS field (Taniguchi et al. 2007), the near-infrared data were from the second data release (DR2) of UltraVISTA survey and the *Spitzer*/IRAC imaging was from S-COSMOS (Sanders et al. 2007). In comparison to S15, the data utilized in this work are 0.3–0.6 mag deeper in the near-infrared $YJHK_s$ filters and $\gtrsim$1.0 mag deeper in the *Spitzer* bands.

3 RESULTS

Postage-stamp cut-out images of CR7 from a selection of the available optical to mid-infrared imaging are shown in Fig. 1. As expected for a $z = 6.6$ galaxy, there is no detection in the optical data at the position of any of the components. In the spectroscopic data, S15 find a spatially compact, continuum detection corresponding to rest-frame wavelengths of 916–1017 Å, which they attribute to Lyman–Werner photons emitted by CR7. We find no strong detection in the Canada–France–Hawaii Telescope (CFHT) *i*-band data, which has a 5σ limiting depth of 26.7 (1.8-arcsec-diameter circular aperture) and is well matched in wavelength to measure such a signal. There is, however, a weak CFHT *i*-band detection to the north of component B. The weak detection is measured to be

[1] Public data release can be found at http://www.eso.org/sci/observing/phase3/data_releases.html

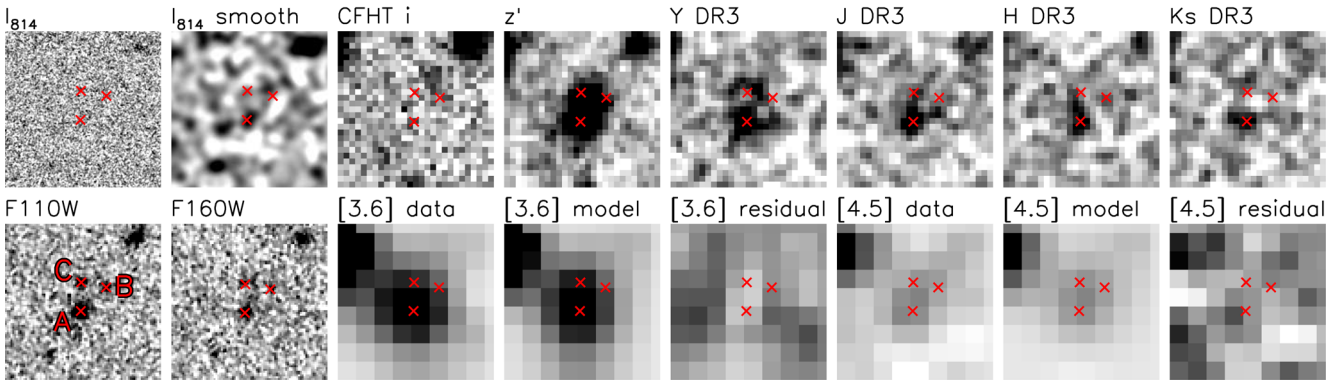

Figure 1. Postage-stamp cut-out images for CR7, showing the deconfusion of the *Spitzer*/IRAC images. The stamps are 5 × 5 arcsec^2 with north to the top and the east to the left. The red crosses show the positions of the three components visible in the *HST*/WFC3 data. The upper row of images from the left- to right-hand side show the *HST*/ACS I_{814} data, at original resolution and smoothed by a Gaussian kernel ($\sigma = 0.15$ arcsec), the ground-based i, z' data from the CFHTLS and Subaru/Suprime-Cam data, and the UltraVISTA DR3 data in the near-infrared bands (Y, J, H, K_s). The lower row of images show the *HST*/WFC3 imaging in the YJ_{110} and H_{160} bands on the left-hand side. The final six stamps show the [3.6] data, the [3.6] model and the residual followed by the similar [4.5] results. For the optical and near-infrared stamps, we have saturated to black any pixel that exceeds the 3σ limit (per pixel), and to white if the pixel value is lower than -1.5σ. For the IRAC stamps of the data and model, we saturate pixels in the same manner but in the range $[-1\sigma, 10\sigma]$, and for the residual stamps, we adjust the range to $[-2\sigma, 2\sigma]$.

$m_{AB} \simeq 28.5$, which is around a 1.5σ detection, and could be a very faint foreground galaxy or a spurious source. The strong z-band detection, which is a combination of continuum emission and Lyman α flux, is peaked at the position of component A (the Pop III/DCBH candidate) and is clearly extended in the direction of components B and C.

3.1 Rest-frame UV emission

In the UltraVISTA DR3 imaging, CR7 is clearly detected in all four filters, and appears spatially extended in the deeper Y and J bands. In thse data, the brightest component A clearly dominates and is visible in the shallower H and K_s stamps. Components B and C are also visible at approximately the 2σ level in the Y and J bands, consistent with the measured magnitudes in the *HST*/WFC3 imaging. To determine the photometry and colour of the Pop III/DCBH candidate, we measured photometry on the ground-based imaging centred on the position of component A using small circular apertures of 1.2 arcsec in diameter. We also measured the photometry in larger apertures of 2 arcsec in diameter to compare directly with the results of S15, and using a diameter of 3 arcsec to provide a more appropriate measure of the total flux. The larger apertures were centred on the peak of the $Y + J$ UltraVISTA image, which is offset by 0.35 arcsec to the north-west of component A (the stamps shown in Fig. 1 are centred on this position). The results are shown in Table 1. All photometry was corrected to total magnitudes assuming a point-source correction.[2] S15 found a strong excess in the J-band photometry for CR7 using the UltraVISTA DR2 data, when the continuum level was derived from fitting to the Y, H and K_s bands. The observed offset of $\Delta m_{AB} = -0.4 \pm 0.13$ mag was interpreted as the contribution to the measured photometry from the spectroscopically observed He II emission line. Converting the J-band excess into an estimated rest-frame equivalent width, S15 inferred an equivalent width of $EW_0 = 80 \pm 20$ Å for the He II line.

[2] For the UltraVISTA images we consider, the enclosed flux for a point source within apertures of diameter 1.2, 2.0 and 3.0 arcsec, respectively, was [Y, J, H, K_s] = [56, 60, 63, 64], [79, 83, 85, 87] and [92, 94, 95, 96] per cent.

Using the deeper near-infrared imaging now available, we find a smaller J-band excess than that determined in S15, with $\Delta m_{AB} = -0.19^{+0.14}_{-0.13}$ for the 1.2-arcsec-diameter measurement. Here, the continuum level was determined from the best-fitting Bruzual & Charlot (2003) SED to the Y, H, K_s and [3.6] bands with the redshift fixed to $z = 6.6$ (as shown in Fig. 2). If, instead, the continuum level in the J band is determined from a power-law fit to the Y, H and K_s bands, we find an excess of $\Delta m_{AB} = -0.17^{+0.14}_{-0.13}$. An offset of $\simeq$0.2 mag was also found using the two larger aperture measurements, and the results are unchanged if point spread function (PSF) homogenized images are used. To understand the differences between our results and those of S15, we compared photometric catalogues from the older DR2 data used by S15 to those from the DR3 data. In the four bands, we find no significant zero-point offset between the two releases, and the aperture magnitudes for CR7 agree within $\lesssim$0.1 mag for the Y, H and K_s imaging. In the J band, however, we find that the measured magnitude for CR7 in the DR3 data is 0.22 mag fainter than in the DR2 imaging. Such an offset is expected for 10 per cent of the objects in this magnitude range due to the photometric errors on the measurement (measured by directly comparing catalogues from the DR2 and DR3 data), and represents an $\sim 1.5\sigma$ deviation from the DR2 value. If we interpret our observed flux excess as due to contamination of this broad-band by an emission line (or lines) at $z = 6.6$, the magnitude of the offset implies an $EW_0 = 40 \pm 30$ Å (using equation 1 in Marmol-Queralto et al. 2016, assuming a filter width of 1740 Å; van der Wel et al. 2011). We note, however, that the near-infrared photometry could also be well fitted by a continuum-only model, given the errors on the photometry. The lower EW_0 we infer is fully consistent with the lower limit calculated from the spectroscopic detection of the likely He II line presented in S15, which implies $EW_0 > 20$ Å.

Comparing our near-infrared photometry in Table 1 to that measured in S15 using an identical aperture (2.0 arcsec diameter), we find good agreement except in the Y band, where our measurement is brighter than the value obtained by S15. In addition, the comparison shows that the photometric errors presented in S15 were underestimated, leading to the very small errors on the derived β value. It is unclear whether S15 used an aperture correction to account for the flux that lies beyond the circular aperture used. If no aperture correction was applied by S15, this would provide a

Table 1. The measured photometry for CR7 utilizing deeper near-infrared data from UltraVISTA DR3 and mid-infrared imaging from the SPLASH survey. The upper part of the table shows the available *HST* and *Spitzer* photometry. For the full object photometry, labelled as component 'Full', the photometry was measured in 3-arcsec-diameter circular apertures on the *HST*/WFC3 data, and the *Spitzer*/IRAC photometry was obtained using a deconfusion analysis based on the UltraVISTA K_s-band data. The lower part of the table shows the ground-based photometry measured in 1.2-, 2.0- and 3-arcsec-diameter circular apertures. Note that the aperture photometry has been corrected to total assuming a point-source correction. The final row of the table reproduces the photometry and β value as measured in S15.

Component	I_{814}	$I_{814}-YJ_{110}$	YJ_{110}	H_{160}	$YJ_{110}-H_{160}$	[3.6]	[4.5]	[3.6] − [4.5]
A	>27.2	>2.2	$25.01^{+0.05}_{-0.05}$	$25.25^{+0.13}_{-0.12}$	$-0.24^{+0.17}_{-0.18}$	$23.79^{+0.10}_{-0.09}$	$24.99^{+0.23}_{-0.19}$	$-1.20^{+0.29}_{-0.32}$
B	>28.2	>1.2	$27.02^{+0.15}_{-0.13}$	$26.88^{+0.30}_{-0.23}$	$+0.14^{+0.38}_{-0.43}$	$25.99^{+0.59}_{-0.38}$	$25.97^{+0.41}_{-0.30}$	$+0.03^{+0.89}_{-0.79}$
C	>28.2	>1.5	$26.67^{+0.10}_{-0.09}$	$26.80^{+0.27}_{-0.22}$	$-0.13^{+0.32}_{-0.37}$	$24.97^{+0.34}_{-0.26}$	$25.56^{+0.45}_{-0.32}$	$-0.59^{+0.65}_{-0.71}$
Full			$24.65^{+0.08}_{-0.07}$	$24.70^{+0.18}_{-0.15}$		$23.49^{+0.10}_{-0.09}$	$24.57^{+0.13}_{-0.12}$	$-1.08^{+0.22}_{-0.22}$

Aperture	i	z'	Y	J	H	K_s	β_{YHK}	Notes
1.2 arcsec	>28.42	$25.24^{+0.11}_{-0.10}$	$25.09^{+0.12}_{-0.11}$	$24.91^{+0.14}_{-0.13}$	$25.10^{+0.20}_{-0.17}$	$24.96^{+0.28}_{-0.22}$	$-1.9^{+0.3}_{-0.3}$	Component A
2.0 arcsec	>27.54	$25.00^{+0.11}_{-0.10}$	$24.71^{+0.11}_{-0.10}$	$24.63^{+0.14}_{-0.12}$	$25.01^{+0.28}_{-0.23}$	$25.16^{+0.34}_{-0.26}$	$-2.5^{+0.3}_{-0.4}$	Full system
3.0 arcsec	>27.10	$24.90^{+0.11}_{-0.10}$	$24.75^{+0.18}_{-0.16}$	$24.68^{+0.21}_{-0.18}$	$24.92^{+0.43}_{-0.31}$	$25.12^{+0.76}_{-0.44}$	$-2.4^{+0.5}_{-0.6}$	Full system
2.0 arcsec	–	$25.35^{+0.20}_{-0.20}$	$24.92^{+0.13}_{-0.13}$	$24.62^{+0.10}_{-0.10}$	$25.08^{+0.14}_{-0.14}$	$25.15^{+0.15}_{-0.15}$	$-2.3^{+0.08}_{-0.08}$	Sobral et al. (2015)

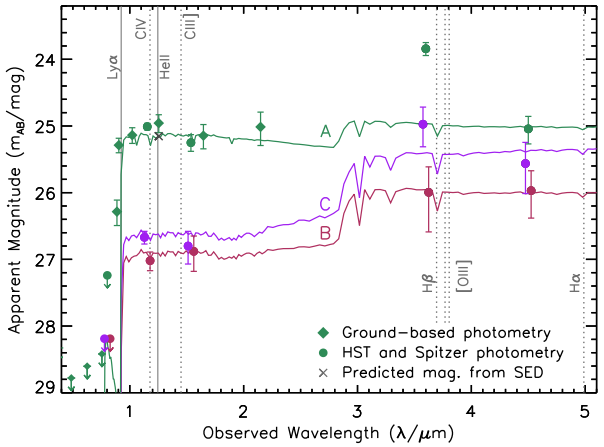

Figure 2. The measured photometry for CR7 from the UltraVISTA DR3 imaging and the deconfused SPLASH data. The *HST* and *Spitzer* photometry is shown as the filled circles, for components A (green), C (purple) and B (red) from the top to bottom. The ground-based photometry is shown for the brightest component A as the filled diamonds. The best-fitting Bruzual & Charlot (2003) model is shown as the solid line in each case, with the predicted model photometry in the J band shown as the black cross (for component A). The solid vertical grey lines show the observed wavelengths of the confirmed Lyα and He II emission lines (S15), whereas the dotted vertical lines show, for reference, the wavelengths of other rest-frame UV and optical lines that have been detected or inferred in other high-redshift LBGs (Smit et al. 2014; Stark et al. 2014, 2015; de Barros et al. 2016).

natural explanation of the differences between our results in the Y band (which shows the largest offset), as the PSF has considerably larger wings in this band than at longer wavelengths and hence requires the largest aperture correction. The apparent agreement between our results and those of S15 in the J band is then a result of our aperture correction approximately matching the ∼0.2 mag offset we find between the DR2 and DR3 photometry (measured from raw, uncorrected aperture photometry). Comparing the S15 photometry to the PSF-homogenized results from the COSMOS15 catalogue (Laigle et al. 2016) supports this interpretation, as the S15 magnitudes are only in good agreement after a wavelength-dependent aperture correction is applied. Our results are in excellent agreement with those measured in the COSMOS15 catalogue, which uses the UltraVISTA DR2 data, except in the J band where we again find an offset of around 0.2 mag as compared to the DR3 photometry. The J-band excess measured from the COSMOS15 catalogue implies an He II equivalent width of $\mathrm{EW}_0 = 100^{+50}_{-40}$ Å, which is again approximately double the value we derive from the deeper UltraVISTA DR3 data.

We measured the rest-frame ultraviolet (UV) slope β ($F_\lambda \propto \lambda^\beta$) of CR7 by fitting a power law to the Y-, H- and K_s-band photometry. The error was calculated from the resulting χ^2 distribution. Even with the deeper UltraVISTA DR3 data, we find the β value to be considerably uncertain. At the position of component A, using small 1.2-arcsec-diameter circular apertures, we find a rest-frame UV slope that is consistent with that found for normal Lyman-break galaxies (LBGs) at high redshift ($\beta = -1.9^{+0.3}_{-0.3}$; Dunlop et al. 2012, 2013; Bouwens et al. 2014). S15 found a bluer value of $\beta = -2.3 \pm 0.08$, with a considerably smaller error despite the shallower UltraVISTA DR2 data used. If we use the same aperture (2 arcsec in diameter), correcting to total magnitudes, we also find a bluer value more consistent with the results of S15 ($\beta = -2.5^{+0.3}_{-0.4}$); however, with more realistic errors (e.g. for similarly bright $z > 6$ LBGs; Bowler et al. 2015). Using the photometry and errors provided for CR7 in the COSMOS15 catalogue, we derive $\beta = -2.4^{+0.4}_{-0.6}$ (2 arcsec aperture). The three β measurements we measure using the UltraVISTA DR3 data (shown in Table 1) are all consistent within the errors; however, we find bluer values for the larger aperture measurements. The slightly bluer values are a result of contamination of the larger aperture photometry in the Y band (which has the most significant PSF wings) by components B and C, which are visible in the UltraVISTA DR3 Y-band imaging as extended emission.

We also measured the photometry and resulting colours for the three individual components from the *HST*/WFC3 imaging. Apertures of diameter 1, 0.4 and 0.4 arcsec were used for components A, B and C, respectively, correcting to a total magnitude assuming a point source. The results are shown in Table 1. There is considerable error in the derived colours due to the faintness of these components in the H_{160} band, but components B and C show colours consistent with a constant F_ν in the rest-frame UV ($\beta \simeq -2$; Fig. 2). We therefore find no evidence that components B and C are particularly red as claimed by S15. Finally, we note that the rest-frame UV colour of component A cannot be robustly inferred from the *HST*/WFC3 photometry because of the contamination of the broad YJ_{110} band by both the Lyman α and likely He II emission lines.

3.2 Rest-frame optical emission

The *Spitzer*/IRAC data analysed in S15 were from the S-COSMOS survey, which is 1 mag shallower than the SPLASH imaging utilized here. As shown in Fig. 1, CR7 is clearly detected in the [3.6] and [4.5] filters in the SPLASH data and appears to show a blue colour in these bands. In Bowler et al. (2014), we analysed the SPLASH data for CR7 (ID 30425) as part of a search for LBGs in the Ultra-VISTA DR2 data. We found that CR7 has a strong blue colour of $[3.6]-[4.5]=-1.4^{+0.5}_{-0.6}$ mag, consistent with the contamination of the *Spitzer*/IRAC filters by rest-frame optical emission lines (e.g. as found by Smit et al. 2014). S15 attributed the majority of the IRAC flux detected in the S-COSMOS imaging to the UV-faint components B and C, as the Pop III model fitted to the brighter component A does not significantly contribute to the *Spitzer* bands.

To investigate further the origin of the rest-frame optical emission in the CR7 system, we have improved on the methodology presented in Bowler et al. (2014) using a deconfusion analysis of the *Spitzer*/IRAC SPLASH imaging. We deconfused the SPLASH imaging using TPHOT (Merlin et al. 2015), using the *HST*/WFC3 YJ_{110} data as the high-resolution input data (our results are unchanged if the H_{160} imaging is used). The best-fitting model from the deconfusion analysis and the residual are shown for the [3.6] and [4.5] bands in Fig. 1. We find that the dominant source of the emission observed in these bands is emitted from component A, not the two fainter components, and that this emission shows a strong blue colour of $[3.6]-[4.5]=-1.2\pm0.3$ (see Table 1). Our results are in good agreement with those presented in Agarwal et al. (2016), who similarly found that 70 per cent of the IRAC emission emanates from component A using a similar methodology. The [3.6] − [4.5] colours measured for components B and C are consistent with zero. To test the results of our deconfusion, we re-ran the analysis masking component A and hence requiring that components B and C are the only sources of the observed IRAC fluxes. The result is an extremely poor fit to the observed data, with a residual of the order of 50 per cent of the peak flux at the position of component A. As we discuss in more detail below, the strong rest-frame optical detection observed for the central component of CR7 is not expected from either a Pop III or a DCBH model, which have SEDs that rapidly decline to longer wavelengths (S15; Agarwal et al. 2016). In addition, these models cannot reproduce the observed blue [3.6] − [4.5] colour, which instead suggests the presence of significant rest-frame optical emission lines in the SED of CR7, including the [O III] λλ4959, 5007 line.

4 DISCUSSION

4.1 The Pop III/DCBH candidate (A)

As observed by S15, it is the brightest component (A) that is the source of the Lyman α and He II emission and hence the Pop III or DCBH candidate. Using our deconfusion analysis, we find that component A has a strong detection in both *Spitzer* bands and shows a blue [3.6] − [4.5] colour. This blue colour cannot be reproduced by pure Pop III or DCBH models, as shown in Fig. 3, where we plot $H_{160}-[3.6]$ against [3.6]−[4.5]. The figure shows the predicted colours of Pop III models derived with the YGGDRASIL code (Zackrisson et al. 2011) and the best-fitting Pop III model presented in S15. The predicted colours from the YGGDRASIL code lie in a tight locus irrespective of the assumed star formation history (burst or constant) and initial mass function (IMF) of the Pop III model or covering

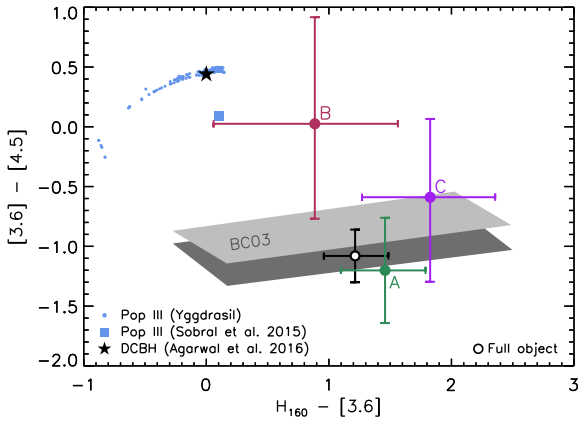

Figure 3. The observed $H_{160}-[3.6]$ and [3.6] − [4.5] colours of the three individual components of CR7 (filled circles) and the full object (open circle), compared to predictions from both standard and exotic models. We show the predicted colours of Pop III models derived from YGGDRASIL (small blue circles) and from S15 (blue square). The DCBH prediction from Agarwal et al. (2016) is shown as the black star. The grey shaded regions show the range of predicted colours from Bruzual & Charlot (2003) models with ages of 10–250 Myr (effectively from the left- to right-hand side), where rest-frame optical emission lines have been added in the range $EW_0(H\beta+[O\,III])=1000$–2000 Å. The light-grey region was calculated assuming a standard ratio of [O III]/H β, whereas the dark-grey region shows the results with [O III]/H $\beta=15$.

fraction ($f_{cov}=0.5$ and 1.0). We show the YGGDRASIL model results determined using a top-heavy IMF ('Pop III.1' and 'Pop III.2' presented in Zackrisson et al. 2011) and with ages less than 50 Myr. In addition, we show the expected colours of the best-fitting DCBH model from Agarwal et al. (2016). The DCBH scenario similarly predicts low [3.6] and [4.5] fluxes and a flat [3.6] − [4.5] colour, in disagreement with the observations.

In contrast, the observed [3.6] − [4.5] colour agrees well with that typically measured for samples of Lyman-break galaxies at $z>6$. In these studies, a blue colour of $[3.6]-[4.5]\lesssim-1.0$ has been observed in both photometric samples (Smit et al. 2014; Roberts-Borsani et al. 2016; Bowler et al. 2017), and for galaxies with a spectroscopic confirmation (Finkelstein et al. 2013; Oesch et al. 2015; Stark et al. 2017). The origin of the blue rest-frame optical colour is believed to be the contamination of these broad-bands by strong nebular-emission lines, with inferred rest-frame EW of $EW_0(H\beta+[O\,III])>600$ Å and potentially reaching in excess of 1800 Å (Smit et al. 2014; Stark et al. 2017). For CR7 at $z=6.6$, the most significant lines are the H β and [O III] λλ4959, 5007 emission lines in the [3.6] band, and the H α line in the [4.5] band (see Fig. 2). Given the canonical ratio of H α to H β of ∼2.87 (Osterbrock & Ferland 2006), we would expect to measure $[3.6]-[4.5]\gtrsim0.0$ if no emission from the [O III] line was present. Instead, we measure a strong blue colour, which is highly suggestive of the presence of the [O III] emission line. In Fig. 3, we show the predicted colours from Bruzual & Charlot (2003) SED models with the H α, H β and [O III] nebular emission lines added assuming a range of EW_0 consistent with that observed for high-redshift LBGs ($1000\leq EW_0\leq2000$ Å). The SED models were created with both exponentially decreasing and constant star formation histories in the age range from 10 to 250 Myr. We assume no dust extinction here, as this would act to move the predicted colours away from the observed blue values.

The observed colours of CR7 can be reproduced (within the errors) with a young starburst model with $EW_0(H\beta+[O\,III])\gtrsim2000$ Å, assuming a standard [O III]/H β ratio for 1/5 $Z_\odot$ (6.3;

Anders & Alvensleben 2003). With this ratio of [O III]/H β, the observations for CR7 shown in Fig. 3 suggest an elevated rest-frame equivalent width of EW$_0$(H β + [O III]) $\simeq$ 2500 Å would provide the best fit to the data. Such a line strength is higher than typically assumed at high redshift, but consistent with the observed colours of lensed galaxies found by Smit et al. (2014). Alternatively, if the [O III]/H β ratio is, in fact, larger at high redshift (as has been suggested in several studies; Curtis-Lake et al. 2013; de Barros et al. 2016; Faisst et al. 2016), then an even bluer [3.6] − [4.5] colour in agreement with that observed for component A can be obtained with EW$_0$ (H β + [O III]) = 2000 Å (we assume [O III]/H β = 15; de Barros et al. 2016). From this simple comparison, we find that young ages (<100 Myr) are required to reproduce the observed rest-frame UV-to-optical colour, H_{160}−[4.5], for the brightest component of CR7 (A), which we find to be flat or slightly blue (at most, the [4.5] filter is boosted by $\Delta m_{\rm AB} \simeq 0.5$ due to H α with our assumed range in EW$_0$). A young age would also be consistent with the observed rest-frame UV slope and the presence of the nebular lines of He II and [O III], which typically require recent star formation within the last ∼10 Myr. In conclusion, the observed rest-frame optical emission for CR7 measured with the *Spitzer* bands at [3.6] and [4.5] excludes a pristine Pop III or DCBH model as presented in the current literature,[3] and is instead typical of $z \simeq 7$ Lyman-break galaxies with strong emission by [O III].

While the rest-frame optical emission of CR7 can be reproduced assuming nebular emission line strengths that are typical of $z \simeq 7$ LBGs, the presence of a strong and narrow He II emission line in the rest-frame UV spectrum of CR7 is unusual in observations of high-redshift LAEs and LBGs (Stark et al. 2014, 2015, 2017; Zabl et al. 2015). To produce He II emission, a very hard ionizing spectrum is required (Stark et al. 2015), and the large equivalent width of EW$_0$ = 80 ± 20 Å derived by S15 is challenging to reproduce with standard enriched stellar population model (Schaerer 2003; Raiter, Schaerer & Fosbury 2010). We find that the UltraVISTA DR3 broad-band photometric data show a lower *J*-band excess, which implies a lower rest-frame equivalent width of He II of EW$_0$ = 40 ± 30 Å, or a line flux of $2.2^{+1.7}_{-1.6} \times 10^{-17}$ erg s^{-1} cm^{-2}, assuming the excess is purely a result of a single line. While these values are consistent with the S15 measurements ($F_{\rm He} = 4.1 \pm 0.7 \times 10^{-17}$ erg s^{-1} cm^{-2}), the lower mean value (and more realistic errors) bring the measured EW$_0$ into the regime that is occupied by more standard interpretations such as active galactic nucleus (AGN) or emission from a low-metallicity starburst. We discuss these interpretations for the CR7 system in the next section. *HST* grism spectroscopy of CR7 (PI: Sobral) will provide a more reliable estimate of the line flux and hence the equivalent width.

4.2 The companion objects (B and C)

Another important component of several of the Pop III and DCBH models for CR7 is the presence of the supposedly older and redder B and C components at close proximity to the Pop III/DCBH candidate (e.g. Pallottini et al. 2015; Agarwal et al. 2016). It is proposed that these companion galaxies provide the required Lyman–Werner radiation to prevent star formation at the site of CR7 and hence keep the gas pristine. Both S15 and Agarwal et al. (2016) claim that these components are red with best-fitting ages of $\gtrsim$300 Myr. Taking into account the considerable errors on the colours of components B and C, we find no evidence that they are particularly red in the rest-frame UV; however, they do show a (relatively uncertain) red H_{160}−[3.6] colour (see Fig. 2). Agarwal et al. (2016) claim that these components cannot be fitted with a single stellar population (SSP) model; however, we find a large range of plausible star-formation histories (including SSPs) that can fit the observed photometry due to the sparse sampling in wavelength (five filters) and the degeneracies present in SED fitting. The lack of acceptable solutions in Agarwal et al. (2016) appears to be a consequence of the assumption of no dust attenuation in the SED-fitting analysis; however, there is no evidence that these components are dust-free. We fit the five-band photometry ($I_{814}, YJ_{110}, H_{160}$, [3.6], [4.5]) for components B and C using a range of SED models including dust attenuation with a maximum of $A_V = 4.0$, assuming a Calzetti et al. (2000) attenuation law, both constant and exponentially declining star formation histories and a Chabrier (2003) IMF (full details are described in Bowler et al. 2014). For both components, the best-fitting model to the photometry is at $z \simeq 6.6$; however, for component B, a lower redshift solution ($z = 1.4$) is formally acceptable. Unsurprisingly, given the large errors on the photometry for these faint components, we find that the ages and masses are considerably uncertain, with best-fitting ages of 200^{+600}_{-180} and 500^{+300}_{-350} Myr for B and C, respectively (computed by fixing the redshift to $z = 6.6$). Note the large uncertainties on these derived ages, which span from several tens of Myr to the age of the Universe at $z = 6.6$, which is again a result of the large photometric errors and, in particular, the degeneracy between age and dust attenuation (e.g. see Curtis-Lake et al. 2013). The masses of components B and C are more constrained than the ages, with best-fitting values of $\log_{10}(M/{\rm M}_\odot) = 9.3^{+0.5}_{-0.6}$ and $9.7^{+0.2}_{-0.3}$, respectively. These masses are considerably different from those determined in Agarwal et al. (2016), illustrating the uncertainties inherent in the SED-fitting process, especially in the case of weak *Spitzer*/IRAC detections in confused imaging.

Finally, we perform SED fitting to the broad-band photometry available for the brightest component A of CR7, using only those filters that are uncontaminated by confirmed or probable, strong line emission. The resulting fits prefer a low age, <110 Myr (1σ), with a mass of $\log_{10}(M/{\rm M}_\odot) = 9.2^{+0.3}_{-0.1}$. Note that the mass estimate here should be seen as an upper limit, as we have fitted to the observed [4.5]-band magnitude, which is likely contaminated by H α emission. Calculating the SFR directly from the UV according to the Madau, Pozzetti & Dickinson (1998) prescription, we find ${\rm SFR}_{\rm UV} \simeq 20\,{\rm M}_\odot\,{\rm yr}^{-1}$.

5 ALTERNATIVE INTERPRETATIONS

In this section, we argue that more standard scenarios for the nature of CR7 are acceptable within the current observational constraints. We consider here two alternative interpretations for CR7: the first being a low-mass, narrow-line AGN and the second being a young low-metallicity starburst, modelled with the inclusion of binary stars.

5.1 Type II AGN

A natural explanation for the presence of He II emission is excitation by an AGN, whose power-law spectrum can extend into the rest-frame near-UV (NUV) and therefore provide the high-energy photons required to ionize Helium ($E = 54.4$ eV). The spectra of AGN typically show fairly weak He II (EW$_0 \lesssim 10$ Å; Vanden Berk

[3] Since the completion of this work, two additional studies have been presented, Agarwal et al. (2017) and Pacucci et al. (2017), which claim to be able to reproduce the observed [3.6] − [4.5] colour of CR7 with a DCBH model.

et al. 2001; Harris et al. 2016); however, stronger emission lines of $EW_0 \gtrsim 30$ Å have been observed in samples of radio-selected and Type II objects at higher redshift (e.g. Stern et al. 2002; Jarvis, van Breukelen & Wilman 2005; Matsuoka et al. 2009). S15 excludes an AGN based on the narrow linewidth measured for He II, the lack of metal lines measured in the near-infrared spectrum, and the limits on the X-ray and radio luminosity. While broad-line AGNs cannot reproduce the width of the He II line in CR7 ($130 \pm 10\,\mathrm{km\,s^{-1}}$), narrow-line-obscured (Type II) AGNs with low-mass black holes ($M_{BH} \simeq 10^6\,M_\odot$) are observed to have similarly narrow lines (e.g. Ludwig et al. 2012), with Greene & Ho (2005) showing that the narrow-line region traces the host galaxy velocity dispersion. The lack of metal lines detected by S15 is also consistent with the range of line ratios exhibited by narrow-line AGNs. In particular, the lack of $NV\lambda1240$ \AA emission has been observed in samples of Type II quasars from the Sloan Digital Sky Survey (Alexandroff et al. 2013) and in high-redshift radio galaxies (Matsuoka et al. 2009).

The measured non-detection of the [C III], C III]$\lambda\lambda$1907, 1909 and O III]$\lambda\lambda$1661, 1666 doublets with a ratio of He II/C III] > 2.4 and He II/O III] $> 2.4\,(1\sigma$; S15) is not sufficient to exclude an AGN either. Indeed, Feltre, Charlot & Gutkin (2016) show that such low ratios are more easily explained by the presence of an AGN rather than stellar processes. There is a large spread in the observed line ratios for AGNs that are consistent with the observations for CR7. For example, a similar C III]/He II ratio can be found in both radio-loud (Jarvis et al. 2001; Matsuoka et al. 2009) and *Spitzer*-selected AGNs (Martinez-Sansigre et al. 2006). We note that from the available ground-based XSHOOTER spectrum, the prevalence of C IV cannot be robustly constrained due to sky-line contamination at 1.18 μm. Type II AGNs typically produce strong Lyman α and rest-frame optical emission lines such as H α, H β and [O III] in agreement with what we infer for CR7 (e.g. Zakamska et al. 2003). In fact, the elevated [O III]/H β ratios typically found for AGNs (e.g. Baldwin, Phillips & Terlevich 1981; Kewley et al. 2006) compared to galaxies would result in a better agreement with the observed $[3.6] - [4.5]$ colour for a similar assumed EW_0 (Fig. 3).

The radio and X-ray imaging in COSMOS is insufficient to exclude a typical moderate-radio-luminosity AGN with the UV luminosity of CR7 (e.g. see a similar analysis for Himiko in Ouchi et al. 2009). The 5σ depth of the Very Large Array 1.4-GHz data in COSMOS is approximately 100 μJy per beam at the position of CR7 (Schinnerer et al. 2010), and hence if CR7 had a similar ratio of UV-to-radio flux as shown in radio-loud quasars known at $z \simeq 6$ (e.g. Zeimann et al. 2011; McGreer et al. 2006), it would be only marginally detected in the available data. Deeper Jansky-VLA imaging in the COSMOS field at 3 GHz (PI Smolčić), which will extend a factor of 3 deeper than the current imaging, will provide greater constraints on the radio emission from CR7. Finally, in the rest-frame UV, as probed at high resolution by the *HST*/WFC3 data, CR7 shows a compact morphology that is consistent with an AGN contribution. Fig. 4 shows the surface-brightness profile of the brightest component of CR7 (A) derived from the YJ_{110} data. Extended flux is evident in the profile; however, the central region is extremely compact and indistinguishable from a point source. While the YJ_{110} filter includes the Lyman α emission line, we expect the surface brightness profile to be dominated by continuum emission. This is because (1) the Lyman α emission is considerably extended (>2 arcsec; S15); and (2) the emission line is at the very blue end of the photometric filter, and hence the continuum flux dominates by around a factor of 3. A similarly compact surface-brightness profile is found in the shallower H_{160} image.

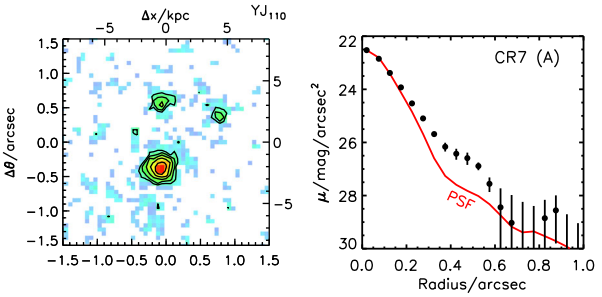

Figure 4. The left-hand figure shows the YJ_{110} data for CR7, scaled by surface brightness. The contours trace 0.5-mag intervals in the range 23.0–25.5 $\mathrm{mag^{-1}\,arcsec^{-2}}$. The right-hand figure shows the surface-brightness profile of the brightest component of CR7 (component A), with the profile of the YJ_{110} PSF shown as the solid red line.

5.2 Low-metallicity starburst

In addition to an AGN, there are stellar sources such as Wolf–Rayet (WR) and hot massive stars that are capable of producing the hard UV photons required to ionize helium (e.g. Kudritzki 2002; Eldridge & Stanway 2009). While significant He II emission is uncommon in the local Universe, the presence of He II in the rest-frame UV spectra of $z = 2$–4 LBGs has been noted by several studies (e.g. Shapley et al. 2003; Allam et al. 2007; Erb et al. 2010). The typically broad He II lines observed, which show $EW_0 \lesssim 7$ Å (Shapley et al. 2003; Cassata et al. 2013), have been explained by the presence of WR stars (Brinchmann, Pettini & Charlot 2008) in these galaxies or alternatively through the consideration of binary star pathways (Eldridge & Stanway 2012). Using the BPASS models, both Eldridge & Stanway (2012) and Steidel et al. (2016) have found that by including massive binary stars in the SED modelling it is possible to reproduce the observed UV spectra of LBGs at $z = 2$–4 (including the diversity in the He II and C IV emission-line strengths; also see Gutkin, Charlot & Bruzual 2016). In general, the BPASS models produce more ionizing radiation over a longer period than in binary-free models (Stanway, Eldridge & Becker 2015). Binary stellar pathways lead to longer lived hot WR-like stars, which enhance the strength and longevity of the broad He II line (Eldridge & Stanway 2009) and, furthermore, lead to an elevated [O III]/H β ratio as has been found in LBGs and Lyman-break analogues (Stanway & Davies 2014; Steidel et al. 2016).

In comparison to CR7, however, there are clear differences between the observed strong $EW_0 = 80 \pm 20$ Å (S15) and narrow ($\Delta v = 130 \pm 20\,\mathrm{km\,s^{-1}}$) line and the He II emission in these lower redshift LBGs. Even with the lower inferred $EW_0 = 40 \pm 30$ Å that we find for CR7 in this study, the line strength is still significantly higher than that found in He II emitters observed at lower redshift, and is more compatible with an AGN origin (Cassata et al. 2013). In addition to the line strength, the width of the line is narrower than the stellar He II emission predicted from the BPASS models, which exceeds $1000\,\mathrm{km\,s^{-1}}$ as a result of strong stellar winds from WR-type stars. In previous studies of the rest-frame UV emission lines produced by stellar population models that do not include binary stars, only with extremely low metallicities ($<10^{-7}\,Z_\odot$; Schaerer 2003, see also Raiter et al. 2010) can the EW_0 value inferred for CR7 be produced. Furthermore, in these models, the He II emission is present only at very young ages, with the EW_0 dropping to essentially zero at $\log(\mathrm{age/yr}) > 6.3$ (fig. 7 in Schaerer 2003). As noted in Eldridge & Stanway (2012) and Erb et al. (2010), however, the BPASS models presented previously do not include nebular line emission. A nebular emission component produces a narrow line, often

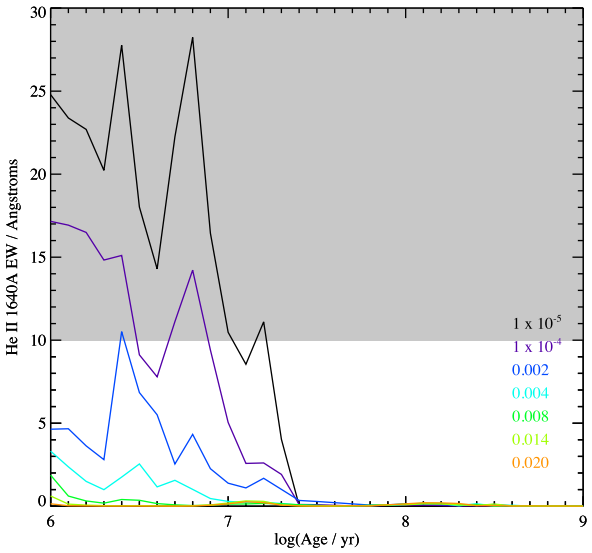

Figure 5. The predicted He II EW for the BPASS SED models described in the text, as a function of age. The grey-shaded region shows the 1σ lower limit on the EW_0 of this line, inferred from the UltraVISTA DR3 data studied here. The coloured lines show a range of different metallicity mass fractions, which correspond to $\simeq Z_\odot$ to $1/2000\ Z_\odot$.

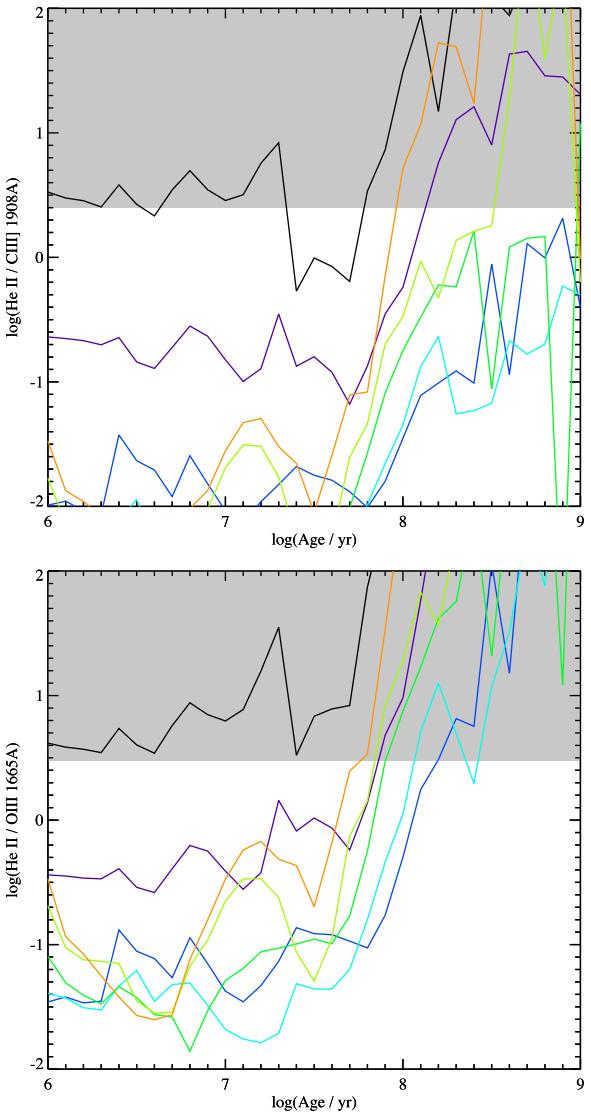

Figure 6. In the upper and lower plots, respectively, we show the He II to C III] and He II to O III] line ratio predicted by the BPASS models described in the text. The grey-shaded region in the lower plot shows the ratios allowed by the observations of CR7 presented in S15, represented by the 1σ upper limit in the C III] or O III] doublet flux. Assuming the lower He II EW_0 found in this study, the limits drop to $\log_{10}(\text{He II/X}) > 0.1(-0.2)$ at 1σ (2σ) for both X = C III] and O III]. As in Fig. 5, the coloured lines show a range of different metallicity mass fractions, which correspond to $\simeq Z_\odot$ to $1/2000\ Z_\odot$.

superimposed on a broader component such as that observed for the $z = 2.3$ low-metallicity star-forming galaxy BX418 studied by Erb et al. (2010). Cassata et al. (2013) also found a population of He II emitters with narrow linewidths, attributing these to either pockets of Pop III star formation or a peculiar stellar population. Before we continue to compare the observed properties of CR7 to predictions of the nebular emission lines from BPASS, we note that an alternative source of the narrow He II emission observed in studies such as Cassata et al. (2013) has been discussed recently by Gräfener & Vink (2015), who explore the emission from very massive stars (VMSs). While we do not discuss such models further in this work, we note that with a moderately low metallicity ($0.01\ Z_\odot$), the VMS models, which include WNh-type stars, can produce strong He II emission with $EW_0 \simeq 20$–40 Å (for single stars), linewidths of a several hundred km s^{-1} and weak metal lines. These particular stellar pathways are not currently implemented in BPASS, and hence potentially their inclusion could further boost the predicted narrow He II component.

5.2.1 *Comparison to the BPASS models*

We investigated the potential strength of the nebular rest-frame UV and optical lines using the latest version of the BPASS models (v2.0; Eldridge et al., in preparation) coupled with radiative transfer effects modelled with CLOUDY (Ferland et al. 2013). The models were generated using the same nebular gas geometry and physical conditions as presented in Eldridge & Stanway (2009) and Stanway & Davies (2014), with an electron density of $10^2\ \text{cm}^{-3}$. A top-heavy IMF was used as described in Stanway et al. (2015), and the gas-phase metallicity was taken to be the same as the stellar metallicity. The models were created assuming an instantaneous burst star formation history. In addition to the recently available BPASS v2.0 models, we include two models at lower metallicities ($1/200$ and $1/2000\ Z_\odot$) that are under development for release in BPASS v2.1. In Fig. 5, we show the expected nebular He II EWs for these models with a range of metallicities (ranging from a mass fraction of 1×10^{-5} to 0.02, or equivalently $1/2000\ Z_\odot$ to $Z_\odot$ assuming a solar metallicity fraction of 0.02). The BPASS models shown at low metallicity predict significantly stronger nebular emission-line strengths for He II than the broad stellar component (typically 1–3 Å; Eldridge & Stanway 2012). In comparison to CR7, the models with young ages up to $\simeq 20$ Myr and low metallicities of $1/200$ or $1/2000\ Z_\odot$ are able to produce line emission consistent with the observed strength, showing $EW_0 \simeq 10$–30 Å. The $1/2000\ Z_\odot$ metallicity model is also consistent with the upper limits on the C III] and O III] emission lines determined observationally in S15 (the lower panels of Fig. 6), although the higher metallicity models struggle to reproduce this ratio at young ages. We note that if the EW_0 of He II is lower than that determined by S15, as we find (see Section 3.1), then this would imply that the upper limits on the He II/C III] and He II/O III] ratios are

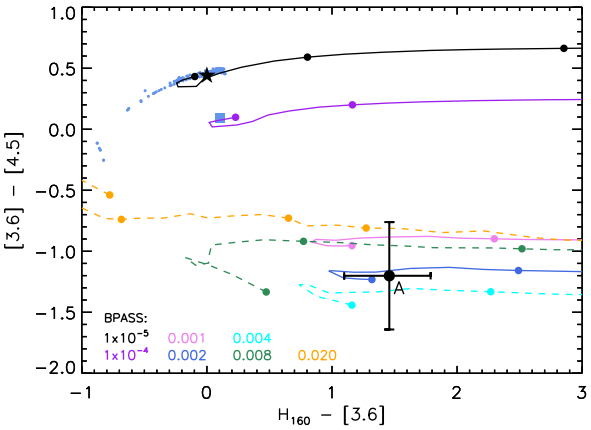

Figure 7. The predicted $H_{160}-[3.6]$ and $[3.6]-[4.5]$ colours of the BPASS models (lines), compared to the observed colours of component A of CR7 (filled black circle). The line colours specify the metallicity mass fraction of the model. For each line, the age increases from the left- to right-hand side, with circles denoting 1, 10, 50 and 100 Myr. Dashed lines show metallicity mass fractions from 0.02 to 0.004 ($\simeq Z_\odot$ to $1/5\,Z_\odot$), which show a trend to a more negative $[3.6]-[4.5]$ colour as the metallicity decreases. As the metallicity drops further, however, the trend is reversed (solid lines; 0.002 to 1×10^{-5} corresponding to $1/10$–$1/2000\,Z_\odot$), and the predicted $[3.6]-[4.5]$ colour eventually becomes positive. The predicted colours of Pop III and DCBH models are shown as the points in the upper right-hand panel, as described in the caption of Fig. 3.

also a factor of 2 less stringent with $\log_{10}(\mathrm{He\,II}/\mathrm{C\,III}]) > 0.1(-0.2)$ at 1σ (2σ) significance. We therefore find that the BPASS models can reproduce the observed rest-frame UV lines of CR7; however, we require that the system has a low-metallicity around $1/2000\,Z_\odot$, given the range of input parameters that we explore in this study.

In addition to the rest-frame UV line strengths and ratios observed in CR7, any model of the system must be able to reproduce the strong emission in the rest-frame optical (from the Balmer and [O III] lines) that we infer from the *Spitzer*/IRAC photometry. In Fig. 7, we show the $H_{160}-[3.6]$ and $[3.6]-[4.5]$ colours predicted by the BPASS models we consider in this study, in comparison to the observed colour of component A of CR7 (the Pop III/DCBH candidate). Above 10 Myr the models show a constant $[3.6]-[4.5]$ with age, as the Hα, Hβ and [O III] emission lines decay with an approximately constant ratio after the initial burst. The large variation in the $H_{160}-[3.6]$ colour with time is predominantly the result of the decay of the H_{160} flux, which probes the far-UV wavelengths ($\lambda_0 \sim 2000$ Å) at $z \simeq 7$. At ages of a few Myr, the predicted colours vary on short time-scales as the galaxy SED is dominated by a small number of the most massive stars, as they progress through the early stages of rotational mixing and quasi-homogeneous evolution (Eldridge & Stanway 2012).

When comparing the predicted and observed rest-frame optical colours for CR7, we find that only models with metallicities of $1/10$–$1/20\,Z_\odot$ and ages of <10 Myr can reproduce the observations for component A. The required age of the models matches well with that required to reproduce the He II EW_0 and the rest-frame UV line ratios; however, the metallicity needed to reproduce the $[3.6]-[4.5]$ colour is higher by around a factor of 100 than that required to produce sufficient He II flux (shown in Fig. 5). This is a result of the lower metallicity models showing dramatically lower [O III] fluxes (e.g. as seen in the predicted [O III]/Hβ ratios in Gutkin et al. 2016), which leads to much redder $[3.6]-[4.5]$ colours in comparison to CR7. We therefore find that the BPASS models that we consider in this study have difficulty reproducing simultaneously the observed strengths of the rest-frame UV and the rest-frame optical line strengths for CR7.

In recent work studying the rest-frame UV and optical spectra of $z \simeq 2.4$ LBGs, however, Steidel et al. (2016) found that to reproduce the full stellar and nebular spectra including the He II and [O III] emission-line strengths required a supersolar O/Fe ratio with $\mathrm{O/Fe} \simeq 5\,(\mathrm{O/Fe})_\odot$. The BPASS model predictions we show in Figs 5–7 were calculated based on solar abundance ratios, and hence may not be an adequate representation of the conditions at high redshift. To test the possible effect of such an increase in the α-element abundances on the predicted line strengths from the BPASS models, we re-ran CLOUDY after the gas-phase abundances of Mg, Ne, O and Si were increased by factors of ∼2–10 times the solar values. For an increase in the O/Fe ratio of $\simeq$10, the predicted [O III] emission (and $[3.6]-[4.5]$ colour) matches that of the BPASS model with a metallicity that is a factor of 10 higher. Hence, the predicted $[3.6]-[4.5]$ colours for the model with a stellar metallicity of $1/200\,Z_\odot$ approximately follow that of the $Z_\star = 1/20\,Z_\odot$ model, while the strength of the He II and Lyman α emission is unaffected. As is evident from Fig. 7, the predicted rest-frame optical line ratios and subsequent $[3.6]-[4.5]$ colour are very sensitive to metallicity between $1/20$ and $1/200\,Z_\odot$, and hence an increase in the O/Fe abundance brings the BPASS models significantly closer to reproducing the $[3.6]-[4.5]$ observed for CR7 (within 2σ for a factor of 5 increase in the O abundance).

In summary, with the particular parameters presented in this comparison, we cannot reproduce both the rest-frame UV and rest-frame optical emission-line strengths with a BPASS (and CLOUDY) model of a single common metallicity and assuming solar element abundance ratios. If, however, at high redshift there is significant α-enhancement as expected for young systems, we find that a BPASS model with $Z_\star = 1/200\,Z_\odot$ can reproduce the He II line strength ($\mathrm{EW}_0 > 10$ Å) and the inferred [O III] line strength (to within 2σ assuming a five-fold increase in the O/Fe ratio; Steidel et al. 2016). With such a model, there is tension with the upper limits on the presence of other rest-frame UV lines, as presented (for Solar abundance ratios) in Fig. 6; however, we caution that these lines can be sensitive to the particular physical conditions input into the photoionization code (e.g. see Stanway & Davies 2014; Feltre et al. 2016). Given the uncertainties inherent in the modelling of nebular emission lines, we conclude that the BPASS models that include binary stars can provide a feasible galaxy model that broadly matches the observational constraints available for CR7. In particular, in comparison to other stellar evolution code predictions, only the BPASS models can currently produce the required nebular He II emission observed in CR7 without an AGN source. With future independent measurements of the He II line strength, stronger upper limits on the presence of C III] and other rest-frame UV lines, and the detection of rest-frame optical lines with the *James Webb Space Telescope (JWST)*, it will clearly be possible to more stringently constrain the stellar populations present in CR7.

6 CONCLUSIONS

We provide improved constraints on the broad-band photometry for CR7 using deeper near-infrared imaging from the DR3 of the UltraVISTA survey, and deeper *Spitzer*/IRAC photometry from the SPLASH data set. The data show that the Pop III/DCBH candidate in the CR7 system shows a strong, blue, rest-frame optical colour as measured by the *Spitzer*/IRAC [3.6] and [4.5] bands. The magnitude and colour of these detections cannot be reproduced by the current

Pop III and DCBH models, and instead imply that the [3.6] band is contaminated by the [O III]λλ4959, 5007 doublet with an inferred rest-frame equivalent width of $EW_0(H\beta + [O\,III]) \gtrsim 2000$ Å. Furthermore, the improved UltraVISTA DR3 near-infrared data show a lower *J*-band excess than previous studies, suggesting that the spectroscopically detected He II emission line has a lower inferred rest-frame equivalent width of $EW_0 = 40 \pm 30$ Å. The observational constraints on the He II and [O III] emission-line strengths are consistent with the properties of a narrow-line low-mass AGN or, alternately, a young low-metallicity $\sim 1/200\,Z_\odot$ starburst when modelled including binary stars and an enhanced O/Fe abundance ratio. However, we find that this starburst model (from the BPASS code) cannot reproduce the current upper limits on the lack of metals in the near-infrared (rest-frame UV) spectrum. In contrast, such ratios of C III]/He II and O III]/He II are to be expected for an AGN source (Feltre et al. 2016). Future observations of CR7 (and other high-redshift galaxies with likely strong rest-frame optical emission) with *JWST* will be able to directly detect the inferred [O III] emission line at $\lambda_{obs} \simeq 3.8$ μm, and through the measured line ratios and widths, will be able to distinguish between an AGN and a low-metallicity star-forming galaxy.

ACKNOWLEDGEMENTS

This work was supported by the Oxford Centre for Astrophysical Surveys, which is funded through generous support from the Hintze Family Charitable Foundation. JSD acknowledges the support of the European Research Council via the award of an Advanced Grant (PI: J. Dunlop), and the contribution of the EC FP7 SPACE project ASTRODEEP (Ref.No: 312725). RJM and DJM acknowledge the support from the European Research Council via the award of a Consolidator Grant (PI: R. McLure). ERS acknowledges support from UK Science and Technology Facilities Council (STFC) consolidated grant ST/L000733/1. MJJ acknowledges support from the UK STFC [ST/N000919/1]. This publication arises from research partly funded by the John Fell Oxford University Press (OUP) Research Fund. ERS and JJE wish to acknowledge the contribution of the high-performance computing facilities and the staff at the Centre for eResearch at the University of Auckland. New Zealand's national facilities are provided by the New Zealand eScience Infrastructure (NeSI) and funded jointly by NeSI's collaborator institutions and through the Ministry of Business, Innovation and Employment Infrastructure programme (http://www.nesi.org.nz). This work is based in part on observations made with the NASA/ESA *HST*, which is operated by the Association of Universities for Research in Astronomy, Inc., under NASA contract NAS5-26555. This work is based on data products from observations made with ESO telescopes at the La Silla Paranal Observatories under ESO programme ID 179.A-2005 and on data products produced by TERAPIX and the Cambridge Astronomy survey Unit on behalf of the UltraVISTA consortium. This work is based in part on observations made with the *Spitzer Space Telescope*, which is operated by the Jet Propulsion Laboratory, California Institute of Technology under a NASA contract.

REFERENCES

Agarwal B., Johnson J. L., Zackrisson E., Labbe I., van den Bosch F. C., Natarajan P., Khochfar S., 2016, MNRAS, 460, 4003
Agarwal B., Johnson J. L., Khochfar S., Pellegrini E., Rydberg C.-E., Klessen R. S., Oesch P., 2017, MNRAS, 469, 231
Alexandroff R. et al., 2013, MNRAS, 435, 3306
Allam S. S., Tucker D. L., Lin H., Diehl H. T., Annis J., Buckley-Geer E. J., Frieman J. A., 2007, ApJ, 662, L51
Anders P., Alvensleben U. F., 2003, A&A, 401, 1063
Baldwin J. A., Phillips M. M., Terlevich R., 1981, PASP, 93, 5
Bouwens R. J. et al., 2014, ApJ, 793, 115
Bowler R. A. A. et al., 2012, MNRAS, 426, 2772
Bowler R. A. A. et al., 2014, MNRAS, 440, 2810
Bowler R. A. A. et al., 2015, MNRAS, 452, 1817
Bowler R. A. A., Dunlop J. S., McLure R. J., McLeod D. J., 2017, MNRAS, 466, 3612
Brinchmann J., Pettini M., Charlot S., 2008, MNRAS, 385, 769
Bruzual G., Charlot S., 2003, MNRAS, 344, 1000
Calzetti D., Armus L., Bohlin R. C., Kinney A. L., Koornneef J., Storchi-Bergmann T., 2000, ApJ, 533, 682
Cassata P. et al., 2013, A&A, 556, A68
Chabrier G., 2003, PASP, 115, 763
Curtis-Lake E. et al., 2013, MNRAS, 429, 302
de Barros S. et al., 2016, A&A, 585, A51
Dijkstra M., Wyithe S., Haiman Z., Mesinger A., Pentericci L., 2014, MNRAS, 440, 3309
Dijkstra M., Gronke M., Sobral D., 2016, ApJ, 823, 74
Dunlop J. S., McLure R. J., Robertson B. E., Ellis R. S., Stark D. P., Cirasuolo M., de Ravel L., 2012, MNRAS, 420, 901
Dunlop J. S. et al., 2013, MNRAS, 432, 3520
Eldridge J. J., Stanway E. R., 2009, MNRAS, 400, 1019
Eldridge J. J., Stanway E. R., 2012, MNRAS, 419, 479
Eldridge J. J., Izzard R. G., Tout C. A., 2008, MNRAS, 384, 1109
Erb D. K., Pettini M., Shapley A. E., Steidel C. C., Law D. R., Reddy N. A., 2010, ApJ, 719, 1168
Faisst A. L. et al., 2016, ApJ, 821, 122
Feltre A., Charlot S., Gutkin J., 2016, MNRAS, 456, 3354
Ferland G. J. et al., 2013, Rev. Mex. Astron. Astrofis., 49, 137
Finkelstein S. L. et al., 2013, Nat, 502, 524
Furusawa H. et al., 2016, ApJ, 822, 46
Gräfener G., Vink J. S., 2015, A&A, 578, L2
Greene J. E., Ho L. C., 2005, ApJ, 627, 721
Gutkin J., Charlot S., Bruzual G., 2016, MNRAS, 462, 1757
Harris D. W. et al., 2016, AJ, 151
Hartwig T. et al., 2016, MNRAS, 462, 2184
Jarvis M. J. et al., 2001, MNRAS, 326, 1563
Jarvis M. J., van Breukelen C., Wilman R. J., 2005, MNRAS, 358, L11
Kewley L. J., Groves B., Kauffmann G., Heckman T., 2006, MNRAS, 372, 961
Koekemoer A. M. et al., 2007, ApJS, 172, 196
Krug H. et al., 2012, ApJ, 745, 122
Kudritzki R. P., 2002, ApJ, 577, 389
Laigle C. et al., 2016, ApJS, 224, 24
Ludwig R. R., Greene J. E., Barth A. J., Ho L. C., 2012, ApJ, 756
McCracken H. J. et al., 2012, A&A, 544, A156
McGreer I. D., Becker R. H., Helfand D. J., White R. L., 2006, ApJ, 652, 157
Madau P., Pozzetti L., Dickinson M., 1998, ApJ, 498, 106
Marmol-Queralto E., McLure R. J., Cullen F., Dunlop J. S., Fontana A., McLeod D. J., 2016, MNRAS, 460, 3587
Martinez-Sansigre A., Rawlings S., Lacy M., Fadda D., Jarvis M. J., Marleau F. R., Simpson C., Willott C. J., 2006, MNRAS, 370, 1479
Matsuoka K., Nagao T., Maiolino R., Marconi A., Taniguchi Y., 2009, A&A, 503, 721
Matthee J., Sobral D., Santos S., Rottgering H., Darvish B., Mobasher B., 2015, MNRAS, 451, 400
Merlin E. et al., 2015, A&A, 582, A15
Oesch P. A. et al., 2015, ApJ, 804, L30
Oke J. B., 1974, ApJS, 27, 21
Oke J. B., Gunn J. E., 1983, ApJ, 266, 713
Osterbrock D. E., Ferland G. J., 2006, Astrophysics of Gaseous Nebulae and Active Galactic Nuclei. Univ. Science Books, Mill Valley, CA
Ouchi M. et al., 2008, ApJS, 176, 301
Ouchi M. et al., 2009, ApJ, 706, 1136

Ouchi M. et al., 2010, ApJ, 723, 869
Ouchi M. et al., 2013, ApJ, 778, 102
Pacucci F., Pallottini A., Ferrara A., Gallerani S., 2017, MNRAS, 468, L77
Pallottini A. et al., 2015, MNRAS, 453, 2466
Raiter A., Schaerer D., Fosbury R. A. E., 2010, A&A, 523, A64
Roberts-Borsani G. W. et al., 2016, ApJ, 823, 143
Sanders D. B. et al., 2007, ApJS, 172, 86
Schaerer D., 2003, A&A, 397, 527
Schinnerer E. et al., 2010, ApJS, 188, 384
Shapley A. E., Steidel C. C., Pettini M., Adelberger K. L., 2003, ApJ, 588, 65
Smidt J., Wiggins B. K., Johnson J. L., 2016, ApJ, 829, L6
Smit R. et al., 2014, ApJ, 784, 58
Smith A., Bromm V., Loeb A., 2016, MNRAS, 460, 3143
Sobral D., Matthee J., Darvish B., Schaerer D., Mobasher B., Röttgering H. J. A., Santos S., Hemmati S., 2015, ApJ, 808, 139 (S15)
Stanway E. R., Davies L. J. M., 2014, MNRAS, 439, 2474
Stanway E. R., Eldridge J. J., Becker G. D., 2015, MNRAS, 456, 485
Stark D. P. et al., 2014, MNRAS, 450, 1846
Stark D. P. et al., 2015, MNRAS, 454, 1393
Stark D. P. et al., 2017, MNRAS, 464, 469
Steidel C. C., Strom A. L., Pettini M., Rudie G. C., Reddy N. A., Trainor R. F., 2016, ApJ, 826, 159
Steinhardt C. L. et al., 2014, ApJ, 791, L25
Stern D. et al., 2002, ApJ, 568, 71
Taniguchi Y. et al., 2007, ApJS, 172, 9
Tilvi V. et al., 2010, ApJ, 721, 1853
van der Wel A. et al., 2011, ApJ, 742, 111
Vanden Berk D. E. et al., 2001, AJ, 122, 549
Visbal E., Haiman Z., Bryan G. L., 2016, MNRAS, 460, L59
Xu H., Norman M. L., O'Shea B. W., Wise J. H., 2016, ApJ, 823, 140
Yajima H., Khochfar S., 2016, MNRAS, 467, L51
Zabl J., Norgaard-Nielsen H. U., Fynbo J. P. U., Laursen P., Ouchi M., Kjaergaard P., 2015, MNRAS, 451, 2050
Zackrisson E., Rydberg C.-E., Schaerer D., Östlin G., Tuli M., 2011, ApJ, 740, 13
Zakamska N. L. et al., 2003, ApJ, 126, 2125
Zeimann G. R., White R. L., Becker R. H., Hodge J. A., Stanford S. A., Richards G. T., 2011, ApJ, 736, 57

APPENDIX A: IRAC DECONFUSION WITHOUT COMPONENT A

In Fig. A1, we show the results of the deconfusion analysis of the *Spitzer*/IRAC data if component A is excluded from the modelling. This situation is advocated by S15, who predict low fluxes in the IRAC bands from component A (the Pop III candidate). Without component A, our deconfusion model works by adjusting the contributions to the [3.6] and [4.5] bands at the positions of components B and C, in an attempt to match the data. Comparing Figs 1 and A1, it can be seen that excluding component A results in significantly larger residuals. This is particularly clear in the [3.6] band, where the best-fitting model without component A is unable to reproduce the data well, resulting in a residual of $\simeq$50 per cent of the peak flux.

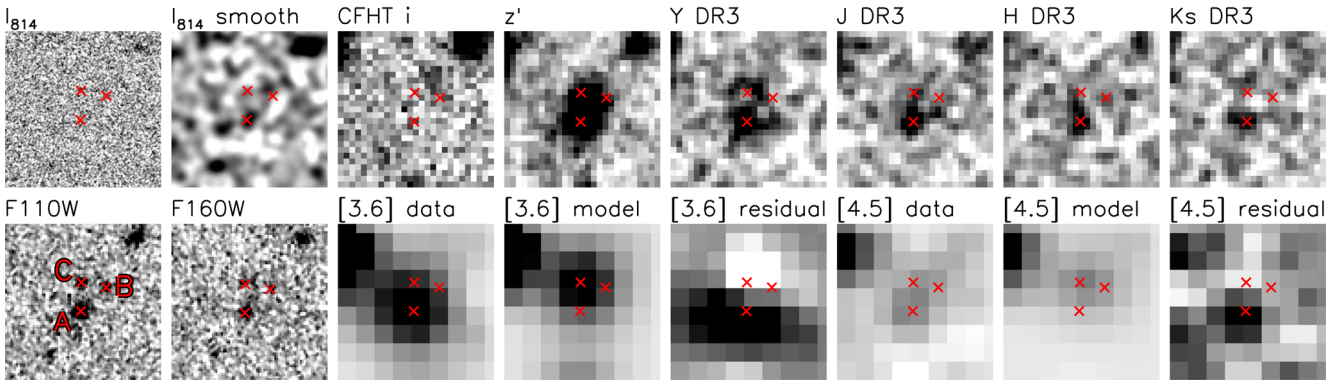

Figure A1. Postage-stamp cut-out images for CR7. Here we show the results of the deconfusion analysis of the *Spitzer*/IRAC images where no contribution from component A is allowed. The size and scaling of the stamps are as described in the caption of Fig. 1. For the IRAC stamps of the data and model, we saturate pixels to black if they exceed the 10σ limit (σ here is per pixel), and to white if they are less than -1σ. The residual stamps are scaled in the same way but in the range of $[-2\sigma, 2\sigma]$.

This paper has been typeset from a TEX/LATEX file prepared by the author.